nature materials

Article

https://doi.org/10.1038/s41563-022-01458-0

Observation of spin-momentum locked surface states in amorphous Bi_2Se_3

Received: 23 February 2021

Accepted: 6 December 2022

Published online: 16 January 2023

Check for updates

Paul Corbae[1,2] ✉, Samuel Ciocys[2,3], Dániel Varjas[4,5], Ellis Kennedy[1,6], Steven Zeltmann[1,6], Manel Molina-Ruiz[3], Sinéad M. Griffin[2,7], Chris Jozwiak[8], Zhanghui Chen[2], Lin-Wang Wang[2], Andrew M. Minor[1,6], Mary Scott[1,6], Adolfo G. Grushin[9], Alessandra Lanzara[2,3] & Frances Hellman[1,2,3]

Crystalline symmetries have played a central role in the identification and understanding of quantum materials. Here we investigate whether an amorphous analogue of a well known three-dimensional strong topological insulator has topological properties in the solid state. We show that amorphous Bi_2Se_3 thin films host a number of two-dimensional surface conduction channels. Our angle-resolved photoemission spectroscopy data are consistent with a dispersive two-dimensional surface state that crosses the bulk gap. Spin-resolved photoemission spectroscopy shows this state has an anti-symmetric spin texture, confirming the existence of spin-momentum locked surface states. We discuss these experimental results in light of theoretical photoemission spectra obtained with an amorphous topological insulator tight-binding model, contrasting it with alternative explanations. The discovery of spin-momentum locked surface states in amorphous materials opens a new avenue to characterize amorphous matter, and triggers the search for an overlooked subset of quantum materials outside of current classification schemes.

Much of materials science and condensed matter physics has focused on exploiting crystal symmetries to understand physical properties, headlined by topological phases and spontaneously broken symmetries in quantum materials. The unusual properties of topological materials, such as the robustness to disorder and their quantized electromagnetic responses, have prompted extensive efforts to classify crystalline topological matter. Non-magnetic crystalline topological insulators and metals with topological bands close to the Fermi level are relatively abundant, representing ~50% of all materials[1], a number that may increase by including magnetic space groups[2]. To identify topological crystals, one asks if the band representations of a particular space group admit a trivial insulator limit compatible with the crystal symmetries; if not, the material is labelled topological. The absence of a crystal lattice places amorphous matter outside this classification, even though it is a subset of materials of comparable size to their crystalline counterpart. This prompts the experimental study of whether or not an amorphous topological insulator exists in the solid state.

Theoretically, amorphous solids can be topological since there are non-spatial symmetries that protect topological phases, such as time-reversal symmetry. In this case, topological states remain robust and do not localize, so long as disorder respects time-reversal symmetry and there is a non-zero mobility gap[3]. Therefore, amorphous materials,

[1]Department of Materials Science, University of California, Berkeley, CA, USA. [2]Materials Science Division, Lawrence Berkeley National Laboratory, Berkeley, CA, USA. [3]Department of Physics, University of California, Berkeley, CA, USA. [4]QuTech and Kavli Institute of NanoScience, Delft University of Technology, Delft, The Netherlands. [5]Department of Physics, Stockholm University, Stockholm, Sweden. [6]National Center for Electron Microscopy, Molecular Foundry, Lawrence Berkeley National Laboratory, Berkeley, CA, USA. [7]Molecular Foundry, Lawrence Berkeley National Laboratory, Berkeley, CA, USA. [8]Advanced Light Source, Lawrence Berkeley National Laboratory, Berkeley, CA, USA. [9]Université Grenoble Alpes, CNRS, Grenoble INP, Institut Néel, Grenoble, France. ✉e-mail: pcorbae@berkeley.edu

https://doi.org/10.1038/s41563-022-01458-0

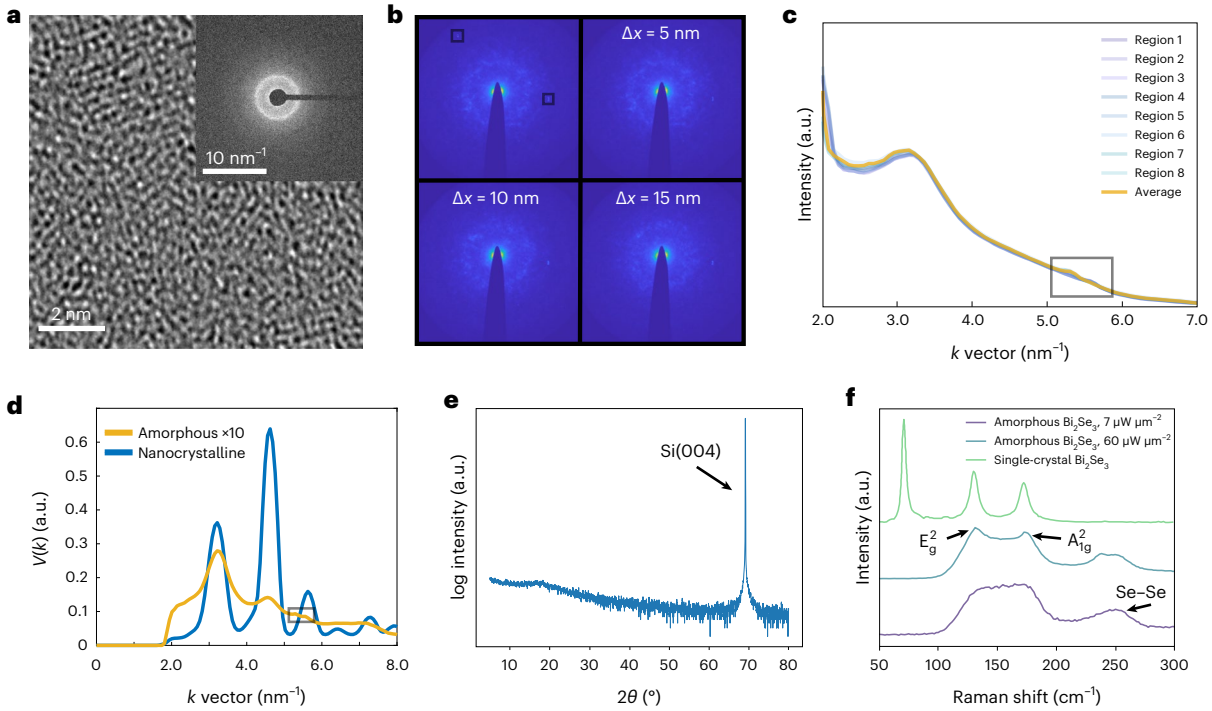

Fig. 1 | Structural and spectral evidence for the amorphous atomic structure of Bi_2Se_3. a, High-resolution TEM image. The inset shows the diffraction pattern for the amorphous Bi_2Se_3 films. We observe a diffuse ring due to the amorphous nature of the film corresponding to ~2.4 Å. **b**, Scanning nanodiffraction patterns taken with a beam spot of 2 nm where each pattern is taken 5 nm apart (each pattern separated by a distance Δx from the first pattern). Each spot shows a speckled ring and no signs of crystallinity. Detector defects are highlighted by the grey boxes. **c**, A one-dimensional intensity cut, $I(k)$, for eight different regions, as well as the average intensity. A peak is observed at ~3.2 nm^{-1}. Detector defects are highlighted by the grey box. **d**, FEM variance, $V(k)$, as a function of scattering vector k for amorphous Bi_2Se_3 (×10 to enable comparison since the magnitude of $V(k)$ is so much smaller) and nanocrystalline Bi_2Se_3. The nanocrystalline sample exhibits substantial variation in intensity for a given k vector from crystalline Bragg diffraction peaks leading to a large variance, while the amorphous sample shows little variation. Detector defects are highlighted by the grey box. **e**, An X-ray diffraction 2θ scan for 100 nm amorphous Bi_2Se_3 after the Se capping layer has been removed showing the same broad, low-angle peak near 17° and no signs of incipient crystallization. X-ray diffraction provides a macroscopic probe of the film structure. The substrate peak is labelled. **f**, Raman spectra for 50 nm amorphous Bi_2Se_3 films using a 488 nm laser. The peaks are each labelled with the respective Raman mode. Different curves (blue and purple) correspond to different laser powers, showing that the bulk Raman modes become more well defined and do not shift. All samples presented in this work show similar spectra to the lower power spectra shown in this figure. Crystalline data[39] (green curve) is overlayed to show the lack of a van der Waals mode at ~72 cm^{-1} in the amorphous films and the extra peak in the amorphous film at ~250 cm^{-1}, which is not seen in crystalline Bi_2Se_3 and is associated with Se–Se bonding.

which lack translational symmetry and cannot be understood in the context of Bloch states, can still present topological properties. Specifically, electrons in a lattice of randomly distributed atoms with strongly disordered electron hoppings—so strong that no memory of a lattice can be used to label the sites—can present topologically protected edge states and quantized Hall conductivity, hallmarks of topological insulators[4–7]. However a solid-state experimental realization is still lacking.

In this work, we have grown and characterized thin films of amorphous Bi_2Se_3. The temperature- and field-dependent resistance reveals the existence of low-dimensional carriers with a reduced bulk contribution. Angle-resolved photoemission spectroscopy (ARPES) and spin-resolved ARPES show a two-dimensional surface state with strong spin-momentum locking. The spin polarization changes with ARPES detection angle, which is proportional to the plane-wave momentum k. In its crystalline form, Bi_2Se_3 is a textbook three-dimensional topological insulator[8]. We find that amorphous Bi_2Se_3, despite being strongly disordered and lacking translational invariance, hosts two-dimensional spin-momentum locked surface states, while nanocrystalline Bi_2Se_3 does not. By numerically simulating a model for amorphous Bi_2Se_3 with trivial and topological phases, we show that dispersive spin-momentum locked surface states exist in amorphous matter with strong spin–orbit coupling, allowing us to discuss their origin.

High-resolution transmission electron microscopy (TEM) on amorphous Bi_2Se_3 thin films (Fig. 1a) shows no signs of crystalline order or even precursor lattice fringes, which would have suggested incipient nanocrystals were starting to form. The diffuse rings in the diffraction pattern in the Fig. 1a inset is typical of amorphous materials with well-defined nearest neighbour coordination and interatomic distance. Energy dispersive X-ray spectroscopy maps (Supplementary Fig. 1) confirm there is no clustering of Bi and Se in our films. To further ensure we are not probing nanocrystalline regions, we performed scanning nanodiffraction, shown in Fig. 1b. Four select beam spots each separated by 5 nm show amorphous speckle[9] and no signs of Bragg peaks (Supplementary Fig. 2). The speckle observed across the Bi_2Se_3 diffraction images is highly uniform, which is indicative of many randomly oriented nanoscale groups of atoms with short-range ordering in the amorphous structure. The diffracted intensity versus scattering vector k for eight different regions is shown in Fig. 1c, with a single peak corresponding to the diffuse diffraction ring. The nearest neighbour spacing set by the ring is 2.39 Å, compared to 3.2 Å in crystalline Bi_2Se_3. Figure 1d presents the normalized variance of the diffracted intensity for amorphous Bi_2Se_3 and nanocrystalline Bi_2Se_3 collected using fluctuation electron microscopy (FEM)[10]. The nanocrystalline sample shows a very large variance from Bragg scattering in crystalline regions with multiple strong peaks due to crystalline order, while the amorphous sample does not, providing clear evidence that the amorphous samples are indeed amorphous. The samples require selenium capping and subsequent decapping in order to preserve the surface for ARPES.

https://doi.org/10.1038/s41563-022-01458-0

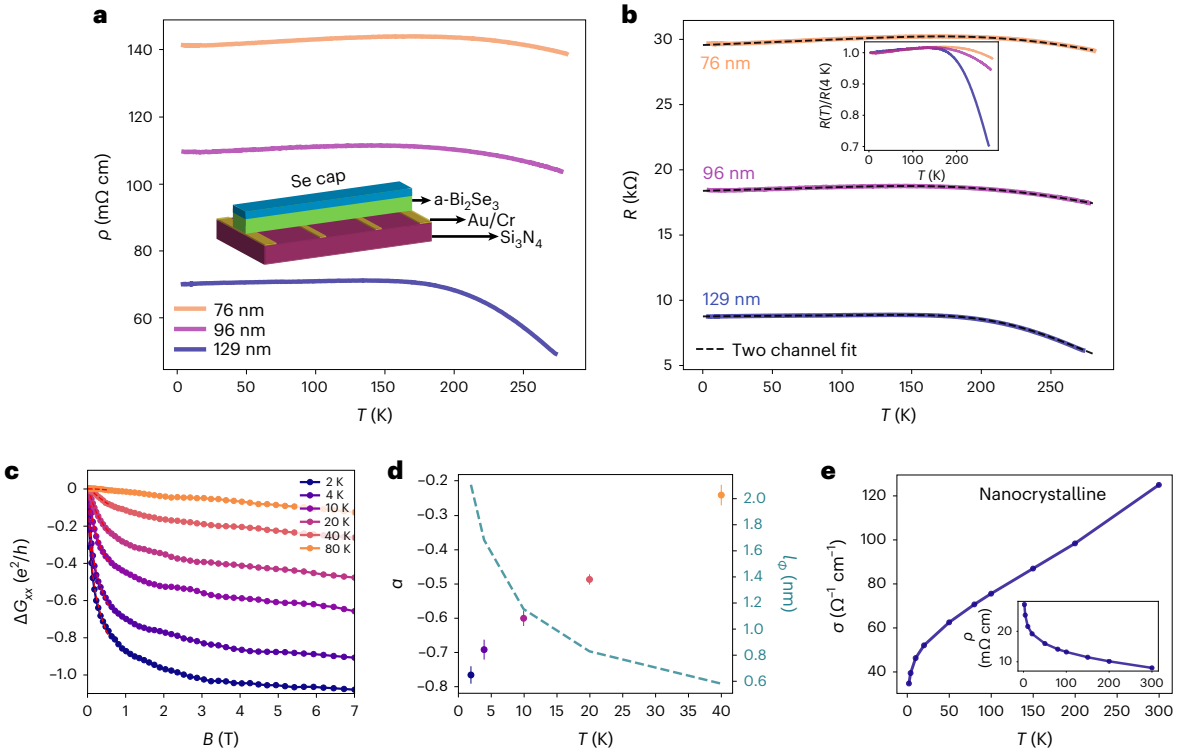

Fig. 2 | Electron transport in amorphous Bi_2Se_3. a, The $\rho(T)$ for 76 nm, 96 nm and 129 nm films. All films show a high resistivity with little temperature dependence. The inset shows a schematic of the structure used to measure resitivity. **b**, The sheet resistance for 76 nm, 96 nm and 129 nm films. All films show high-temperature variable range hopping behaviour (inset shows sheet resistance scaled by the resistance at 4 K) and low-temperature metallic behaviour in R with a low-temperature saturation. Two-channel conductance fits the data reasonably well, indicating a metallic surface and insulating variable range hopping bulk behaviour. **c**, Conductance change as a function of the magnetic field for a 140 nm film, measured at 2 K, 4 K, 10 K, 20 K, 40 K and 80 K, where $\Delta G_{xx} = G(B) - G(0)$. The deep cusp in the low-field regime is characteristic of the weak anti-localization effect. **d**, Magnetoconductance Hikami–Larkin–Nagaoka fits (data points, with colours matching those in **c**) showing α values that indicate decoupled surface surface states at 2 K and a single conduction channel at 20 K. The dephasing length l_φ (blue dashed line) decreases with increasing temperature. Error bars for the fitting parameters are calculated by taking the square root of the covariance matrix. **e**, Nanocrystalline Bi_2Se_3 conductivity (σ) as a function of temperature. The conductivity drops with decreasing temperature. Resistivity is shown in the inset.

To verify that the decapping process does not generate nanocrystalline regions, Fig. 1e displays an X-ray diffraction spectrum for amorphous Bi_2Se_3, showing a strong substrate peak and a low-angle bump typical of amorphous materials that lack long range order but still maintain a well-defined interatomic spacing. Electron diffraction confirms that the decapped film is still amorphous (Supplementary Fig. 2). The Raman spectrum (Fig. 1f) shows two peaks between 135 cm^{-1} and 174 cm^{-1} that correspond to the bulk E_g^2 and A_{1g}^2 vibrational modes, respectively. The A_{1g}^1 van der Waals mode at ~72 cm^{-1}, which is created by the layered structure of the crystal, is absent in our samples. Instead, we observe a peak at 238 cm^{-1} that is not present in crystalline Bi_2Se_3, which we attribute to amorphous Se–Se bonding as seen in Se films[11]. The Raman peaks broaden compared to the crystalline system; the full-width at half-maximum of the E_g^2 mode is 23.7 cm^{-1} compared to 8.0 cm^{-1} (ref. 12). These results show that our samples are amorphous and, while lacking a layered structure with a van der Waals gap, have a local bonding environment similar to the crystalline phase.

Figure 2a,b shows the temperature-dependent transport data for different thicknesses in amorphous Bi_2Se_3, as well as those for the nanocrystalline Bi_2Se_3 (Fig. 2e). The resistivity (ρ) and sheet resistance (R) are shown in Fig. 2a,b. The values (~70–140 mΩ cm and ~8–30 kΩ) are larger than in the crystalline system (~1–2 mΩ cm and ~5–250 mΩ (ref. 13)). The amorphous system also demonstrates a much weaker temperature (T) dependence than the crystalline counterpart[14]. As is typical in amorphous metals, the carrier mean free path is determined more by disorder-driven localization than phonon interactions, leading to a largely temperature-independent resistivity[15]. Moreover, the high resistivity and the weak temperature dependence is inconsistent with either a purely metallic or purely insulating material, and suggestive of a metallic surface on a localized bulk state. The low temperature values are similar to those of bulk insulating topological insulators when gated to bring the Fermi level into the bulk gap[16,17]. The low-temperature $R(T)$ values vary with thickness, possibly a result of small variations in composition between sample thicknesses (<1 at.% deviation) or thickness-dependent defect formation[13]. Transport and ARPES results were reproducible on different samples. The conductivity in nanocrystalline Bi_2Se_3 (shown in Fig. 2e) drops over the entire temperature range and does not display any metallic behaviour with temperature.

The magnetoconductance provides another means to probe the transport. Figure 2c shows magnetoconductance data for a 140 nm film, revealing a sharp decrease in the low-field magnetoconductance ΔG (<2 T) at low temperatures, which is typical of weak anti-localization[18]. The magnetoconductance can be fit with the standard Hikami–Larkin–Nagaoka formula for weak anti-localization[19], $\Delta G(B) = \alpha \frac{e^2}{\pi h}\left[\Psi\left(\frac{\hbar}{4eBl_\phi^2} + \frac{1}{2}\right) - \ln\left(\frac{\hbar}{4eBl_\phi^2}\right)\right]$ where Ψ is the digamma function; B is the out-of-plane field; e is the electron charge; h is Planck's constant; $\hbar$ is the reduced Planck's constant; and l_ϕ (the phase coherence length) and α are used as fitting parameters. According to this model, each conductance channel with a π Berry phase should contribute an $\alpha = -1/2$ factor to ΔG (ref. 20). Fitting our low-field data (Fig. 2d) at 2 K gives a value of $\alpha = -0.81$, suggesting we have two decoupled

https://doi.org/10.1038/s41563-022-01458-0

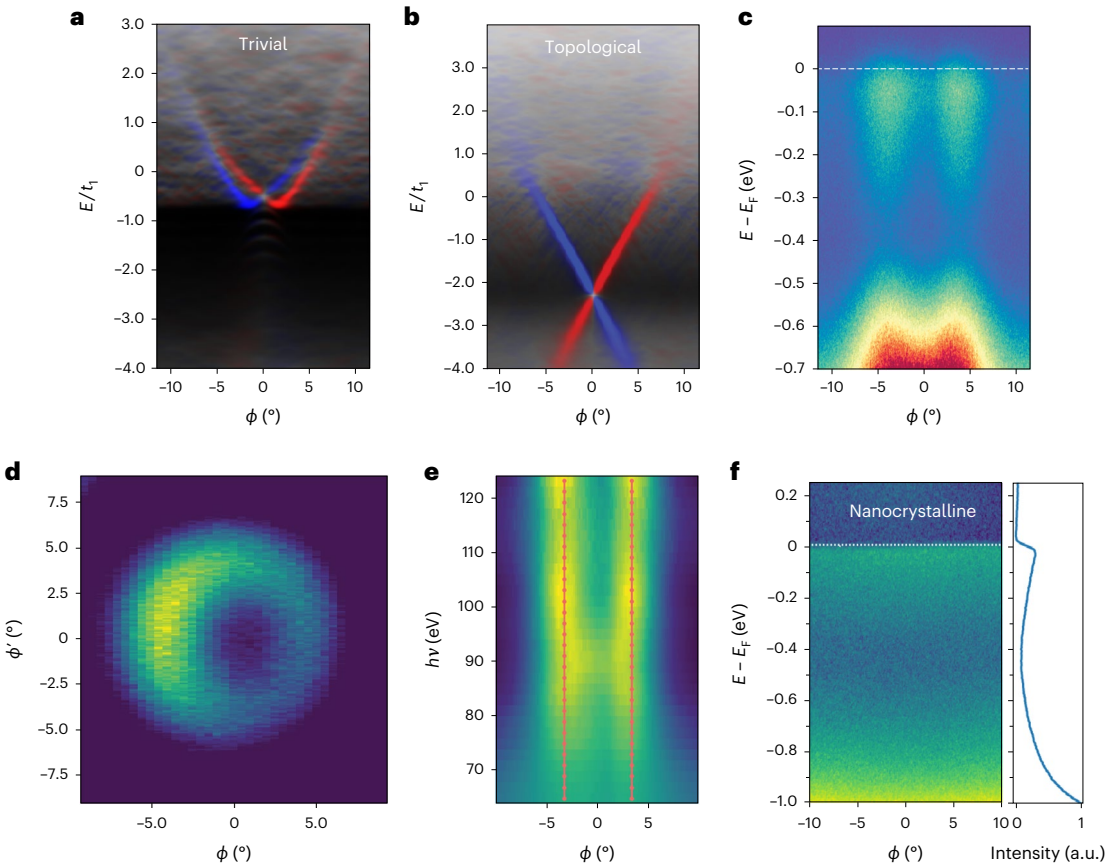

Fig. 3 | ARPES spectra of electronic states in amorphous Bi_2Se_3. **a**,**b**, A calculated spin-resolved surface spectral function as a function of ϕ for the trivial (**a**) and topological (**b**) phases. In the topological phase the Dirac point is low in binding energies and Rashba spin-split states develop near the Fermi level. The energy is normalized by the hopping amplitude t_1. **c**, ARPES spectrum E versus ϕ taken at normal emission at $h\nu = 117.5$ eV. The spectrum reveals vertical states that cross the bulk gap and meet at −0.6 eV near the bulk valence states. **d**, The ring-like in-plane Fermi surface. The ϕ are the angles simultaneously collected by the detector, referenced to normal incidence at a given sample tilt ϕ'. **e**, The $h\nu$ versus ϕ plot with binding energy integrated from −0.6 eV to the Fermi level and normalized by photon energy. The $h\nu$ versus ϕ plot displays no photon energy dependence of the photoemission angle. Red dotted lines are fit to intensity peaks in the $h\nu$ versus ϕ spectrum. **f**, ARPES spectrum E versus ϕ for nanocrystalline Bi_2Se_3 showing an obvious lack of dispersion. The angle integrated intensity is shown as a function of binding energy on the righthand side.

surface states[21]. At 20 K, $\alpha = -0.51$, suggesting the surface states are coupled to a bulk state, causing the entire film to act effectively as one channel, as seen in crystalline Bi_2Se_3 from 2 nm to 100 nm (refs. 22, 23). The observed behaviour in the amorphous Bi_2Se_3 sheet resistance and magnetoresistance is a result of metallic surface states that dominate over a wide range of temperatures.

Based on Hall measurements (Supplementary Fig. 3), the two-dimensional carrier density is $n_{2D} = 2.8 \times 10^{14}$ cm^{-2} and the three-dimensional carrier density is $n_{3D} = 1.9 \times 10^{19}$ cm^{-3}, leading to a mobility (μ) of 21.8 cm^2 V^{-1} s^{-1}. According to the Ioffe–Regel criterion, amorphous Bi_2Se_3 has $k_F l \approx 1$ where k_F is the Fermi wavevector and l the mean free path (ref. 24) with similar μ and n_{3D} values to the bulk, insulating BiSbTeSe solid solution[25]. Additionally, the calculated mean free path at 2 K is ~1 nm. This n_{3D} likely places the Fermi energy (E_F) into the conduction band (seen in the ARPES presented in the following), although the depth depends on the effective mass[24]. Since our system is amorphous, the bulk carriers are expected to be localized and provide little contribution to transport, leading to the observed high resistivity.

Amorphous materials are not expected to have any electronic states with well-defined momenta, but are nonetheless known to support metallic conduction and superconductivity. Since the nearest neighbour distance is well defined (inset in Fig. 1a), there exists a good reciprocal length scale. If sharp spectral features are observed, there exist states with good momentum quantum numbers since this corresponds to the overlap of the electronic wavefunctions with plane waves of well-defined k, modulated by matrix elements. The coordinates θ and ϕ are experimentally measured and refer to the respective angles of photoemission from the sample surface. The plane-wave components k_x and k_y are proportional to θ and ϕ at small angles, where θ is the azimuthal angle and ϕ is the polar angle. In our work, we refer to spin-momentum locking as the spin asymmetry around zero angle since at small angles, the momentum of the plane wave is proportional to the detection angle.

To interpret our experimental data and determine if they are consistent with a topological bulk, we developed a numerical model that realizes a Dirac-like state in the absence of crystalline symmetry (Methods and Supplementary Note 4). In the trivial phase, we observe spin-split states symmetric around $\phi = 0$ above the gap, while in the topological state, a Dirac cone pinned to $\phi = 0$ is visible, guaranteed by time-reversal symmetry, spanning the bulk gap (Fig. 3a,b). Figure 3c displays the raw ARPES spectrum as a function of energy and emission angle ϕ at a specific θ, a momentum space slice that intersects the gamma point, Γ ($\phi = 0°$). The dispersion revealed here in amorphous Bi_2Se_3 marks the first observation of an amorphous band structure with sharp, momentum-dependent features. Notably, the dispersion exhibits two vertical features at the Fermi level crossing the bulk gap. The raw spectrum reveals an intensity peak near E_F starting at −0.2 eV and a sharp rise in intensity below −0.5 eV. The increased intensity of

https://doi.org/10.1038/s41563-022-01458-0

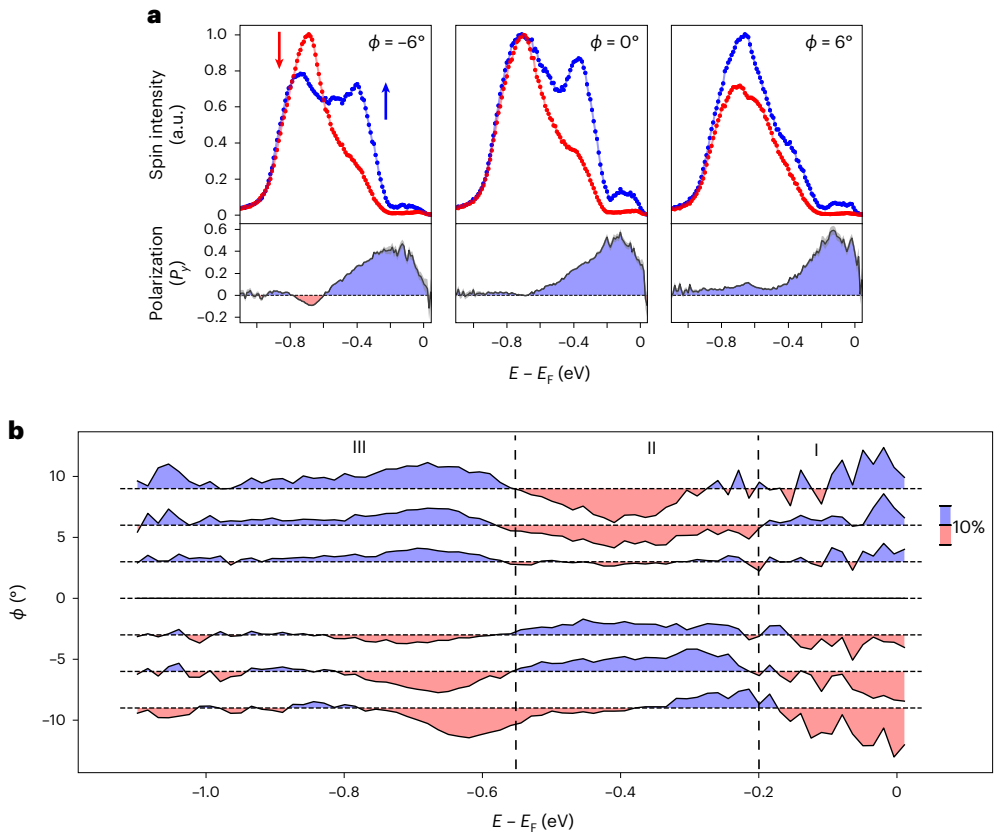

Fig. 4 | Spin-resolved ARPES spectra of electronic states in amorphous Bi_2Se_3. **a**, Spin-resolved energy distribution curves taken at $\phi = -6°$, Γ and $\phi = 6°$. The spin contributions at each binding energy vary with respect to $\phi = 0°$. The top panel displays the spin intensity as a function of binding energy and the bottom panel displays the spin polarization (P_y) as a function of binding energy. Red corresponds to spin-down and blue corresponds to spin-up in all panels. **b**, Spin-resolved energy distribution curve map of E versus ϕ with spin-dependent photoemission matrix element background subtraction taken from $\phi = -9°$ to $\phi = 9°$. The spin polarization switches from red to blue (or vice versa on the other side of Γ) at −0.2 eV and from blue to red at −0.55 eV. Scale bar represents 10% spin polarization.

the surface states near E_F may be due to photoemission enhancement from the less-visible bulk conduction band (Supplementary Fig. 5). The increased intensity below −0.5 eV coincides with a less-dispersive band that is most likely the bulk valence band. The exact bottom of the conduction band and top of the valence band is obscured in the ARPES spectra due to intrinsic broadening; we roughly estimate the bandgap to be ~350 meV via ARPES (Supplementary Note 6).

Figure 3d presents the experimental in-plane Fermi surface in amorphous Bi_2Se_3. The annular Fermi surface is consistent with crystalline Bi_2Se_3, where the dispersion associated surface state in Fig. 3c produces a ring at the Fermi surface. The dot product of the *p*-orbital axis and the experimental coordinates is well defined and should lead to a similar scenario as seen in the crystalline case, in which *p*-polarized light couples asymmetrically across $k = 0$, leading to the observed orbital effect in the Fermi surface. To confirm that these states are localized to the surface, in Fig. 3e we show the photon energy plotted versus emission angle ϕ. Due to conservation of energy, the photon energy ($h\nu$, where ν is the photon's frequency) and k^2 of the photoemitted electron are nearly proportional for large $h\nu$. In the plane (k^2, ϕ) the states are nearly independent of photon energy (red dotted lines in Fig. 3e). For a three-dimensional amorphous system, bulk states must be spherically symmetric and independent of ϕ due to the absence of an average preferred direction. Therefore the strong ϕ dependence and $h\nu$ independence suggest the electrons are not from the bulk and instead originate from surface states. These observations motivate us to interpret these states as two-dimensional surface states.

The presence of strong spin–orbit coupling added to broken inversion symmetry at the surface in our system should lead to a spin texture. Figure 4 shows spin-resolved ARPES taken with 11 eV photons. We observe an anti-symmetric spin polarization, the first observation in an amorphous system, to the best of our knowledge. The spin-polarized energy distribution curves with *p*-polarized light are shown in Fig. 4a at $\phi = -6°$, 0° and 6°. The most evident feature from the three spin-polarized energy distribution curves is the large positive polarization between −0.6 and 0.0 eV that reaches a maximum of ~50%. This large polarization offset is due to spin-dependent photoemission matrix elements in which spin–orbit coupling leads to selective emission of electrons with a particular spin state. This is observed in crystalline Bi_2Se_3 near the upper Dirac cone with similar intensity[26].

Figure 4b presents the spin polarization as a function of binding energy and ϕ after performing the spin-dependent photoemission matrix element background subtraction[26]. From this spin-polarized map, three ranges of binding energy demonstrate distinct anti-symmetric spin polarizations with respect to ϕ: E_F to −0.20 eV (region I), −0.20 eV to −0.55 eV (region II) and −0.55 eV to −0.75 eV (region III). The spin polarization has a magnitude of ±15% and changes sign between these ranges as a function of binding energy. By comparing Fig. 4b with the spin-integrated spectrum in Fig. 3c, we see that region I corresponds to the conduction band, region II corresponds to the in-gap states and region III corresponds to the valence band. The in-gap states of region II have opposite spin polarization to both the conduction band and valence band, suggesting that these states are

indeed separate features from regions I and III and not a consequence of inelastic scattering from region I states or from local variations in composition. The measured spin polarization matches the expected spin polarization from our tight-binding model shown in Fig. 3b for the topological case, with region I representing the spin texture of the trivial Rashba split bulk states near the Fermi level, region II representing the spin texture of the upper Dirac cone of the topological surface state in the bulk bandgap and region III representing the spin texture of the lower Dirac cone within the bulk valence band. We conclude that the two-dimensional surface states form a node around −0.55 eV, and the anti-symmetric spin-resolved spectrum around Γ at E_F is associated with trivial states with a large component at the surface stemming from Rashba-type spin splitting in our system, as seen also in crystalline Bi_2Se_3 (ref. 27).

Our data are consistent with a spin-momentum locked two-dimensional surface state for which we discuss two main origins: non-topological and topological. In the latter, a topological bulk state in amorphous Bi_2Se_3 would produce the dispersive, spin-momentum locked surface states we observe. In this interpretation, the topological surface states cross the bulk gap, as in Fig. 3b, forming a Dirac state similar to the surface states observed in related topological insulator crystals[28]. In the amorphous case, however, the Dirac point can be hidden underneath the bulk valence band due to a strong surface potential[29] (recall that, although a Dirac node crossing is a protected feature of topological insulators, the binding energy of the node is not). Additionally, from our tight-binding model, we expect trivial spin-split states of a Rashba type to develop at the Fermi level, with opposite polarization from the topological surface state, due to broken inversion symmetry at the surface, as observed in the literature[27]. For the topological explanation to be viable, we need to discard the idea that the amorphous spectrum is a result of averaging over nanocrystalline domains. Figure 3f shows the resulting spectrum from nanocrystalline Bi_2Se_3 in which averaging over randomly rotated domains leads to angle-independent photoemission. Our spectrum is also distinct from the crystalline spectrum[27], where the amorphous Bi_2Se_3 spectral features extend further in ϕ than the crystalline case.

Although the topological origin of the surface state is consistent with our data, it is important to discuss non-topological origins like two-dimensional Rashba states, and features that are not captured by our model. Spin-resolved ARPES shows an anti-symmetric spin polarization on either side of the nodal region observed at −0.55 eV. In the topological scenario these would be attributed to a spin-polarized two-dimensional topological surface state. Another possible explanation is that the lack of inversion symmetry at the surface gives rise to trivial Rashba states, as in Fig. 3a, and a spin polarization in the bulk conduction and valence bands. If the spin texture were a result of Rashba splitting, then each near-vertical branch would need to be a single parabolic-like band that returns to the Fermi level. This is because each near-vertical feature has only one spin character and could be plausible if the parabolic dispersion was obscured by the momentum broadening. It would also imply a gigantic Rashba momentum offset of $k_0 \approx 0.4$ Å^{-1}. For reference, the giant Rashba splitting in bulk BiTeI is demonstrated by $k_0 = 0.051$ Å^{-1} (ref. 30), nearly a factor of ten smaller (Supplementary Fig. 7). While we cannot definitively settle on either explanation, the topological scenario seems simpler as it could explain the spin switching of all regions in Fig. 4, and because it seems that a gigantic Rashba splitting is needed to explain our results otherwise. Regardless of the explanation, our observation of well-defined, spin-momentum locked dispersing surface states opens a new direction to characterize amorphous matter and to search for new materials with advantageous properties, such as spin-momentum locking.

In the raw spectra, ARPES features are perceived as near-vertical, yet the underlying bands need not have infinite electron velocity. They are broadened to the point that the electron velocity is hard to quantify, yet we know they do have an increased Fermi velocity compared to the crystal (Supplementary Fig. 8). It is known that the surface environment can affect the location of the Dirac node and the curvature of the bands substantially in the crystalline case[31]. We expect that this is exacerbated in the amorphous case due to the presence of dangling bonds. In fact, amorphous materials have been predicted to experience large band renormalizations that lead to backbending of the dispersions as well as vertical features[32–34]. Combining these factors, it is reasonable to expect large deviations in the amorphous surface state dispersion from the crystalline case, both in the observed band velocity from renormalizations and in the burying of the Dirac node in the valence band. However, the spin polarization allows us to argue that states crossing the gap-like region (II) are unrelated to broadening caused by inelastic scattering of conduction band electrons. Specifically, the spin polarization reverses sign going down in energy from the conduction band (I) at E_F into the gap-like region (II), reversing again in the valence band (III) states.

TEM and Raman data suggest that the local structures of amorphous and crystalline Bi_2Se_3 are similar, which may explain why the topological nature is preserved in the amorphous state[6]. In some cases the amorphous phase of a topological insulator has been shown to be trivial[35]. There is no continuous pathway from the crystalline phase to the amorphous phase but instead a discontinuous phase transformation associated with the nucleation of crystalline domains[36]. The atomic disorder at the grain boundary explains why nanocrystalline Bi_2Se_3 has been shown to be topologically trivial (Fig. 2e, Supplementary Note 7 and Supplementary Fig. 10) (ref. 37).

In conclusion, we have found that amorphous Bi_2Se_3 hosts a dispersing two-dimensional metallic surface state with spin-momentum locking. This experimental observation of spin-momentum locked surface states in an amorphous solid-state system highlights the idea that searching for exotic states in new quantum materials, such spin-momentum locked states, or for topological properties should not be restricted to crystalline solids. Our work provides a study of an amorphous solid-state system with chemical specificity and local bonding environments, a system that can be implemented into devices. To the best of our knowledge there have been no previous reports of ARPES or spin-resolved ARPES on an amorphous solid. Our results represent the first step towards realizing, in real materials, recently proposed non-crystalline topological phases[6,38] that lie outside the known classification schemes for topological crystalline matter[1,2] and that may be more robust than their crystalline counterparts[7]. We expect our work to motivate an effort to understand topological amorphous matter, enabling materials discovery that can provide a path towards affordable and better implementation into modern thin-film processes.

Online content

Any methods, additional references, Nature Portfolio reporting summaries, source data, extended data, supplementary information, acknowledgements, peer review information; details of author contributions and competing interests; and statements of data and code availability are available at https://doi.org/10.1038/s41563-022-01458-0.

References

1. Vergniory, M. G. et al. A complete catalogue of high-quality topological materials. *Nature* **566**, 480–485 (2019).
2. Watanabe, H., Po, H. C. & Vishwanath, A. Structure and topology of band structures in the 1651 magnetic space groups. *Sci. Adv.* **4**, eaat8685 (2018).
3. Hasan, M. Z. & Kane, C. L. *Colloquium*: topological insulators. *Rev. Mod. Phys.* **82**, 3045–3067 (2010).
4. Agarwala, A. & Shenoy, V. B. Topological insulators in amorphous systems. *Phys. Rev. Lett.* **118**, 236402 (2017).
5. Mitchell, N. P., Nash, L. M., Hexner, D., Turner, A. M. & Irvine, W. T. M. Amorphous topological insulators constructed from random point sets. *Nat. Phys.* **14**, 380–385 (2018).

6. Marsal, Q., Varjas, D. & Grushin, A. G. Topological Weaire–Thorpe models of amorphous matter. *Proc. Natl Acad. Sci. USA* **117**, 30260–30265 (2020).
7. Spring, H., Akhmerov, A. R. & Varjas, D. Amorphous topological phases protected by continuous rotation symmetry. *SciPost Phys.* **11**, 22 (2021).
8. Zhang, H. et al. Topological insulators in Bi_2Se_3, Bi_2Te_3 and Sb_2Te_3 with a single Dirac cone on the surface. *Nat. Phys.* **5**, 438–442 (2009).
9. Treacy, M. M. J., Gibson, J. M., Fan, L., Paterson, D. J. & McNulty, I. Fluctuation microscopy: a probe of medium range order. *Rep. Prog. Phys.* **68**, 2899–2944 (2005).
10. Voyles, P. & Muller, D. Fluctuation microscopy in the stem. *Ultramicroscopy* **93**, 147–159 (2002).
11. Lucovsky, G., Mooradian, A., Taylor, W., Wright, G. & Keezer, R. Identification of the fundamental vibrational modes of trigonal, α-monoclinic and amorphous selenium. *Solid State Commun.* **5**, 113–117 (1967).
12. Zhang, J. et al. Raman spectroscopy of few-quintuple layer topological insulator Bi_2Se_3 nanoplatelets. *Nano Lett.* **11**, 2407–2414 (2011).
13. Kim, Y. S. et al. Thickness-dependent bulk properties and weak antilocalization effect in topological insulator Bi_2Se_3. *Phys. Rev. B* **84**, 073109 (2011).
14. Analytis, J. G. et al. Two-dimensional surface state in the quantum limit of a topological insulator. *Nat. Phys.* **6**, 960–964 (2010).
15. Gunnarsson, O., Calandra, M. & Han, J. E. *Colloquium*: saturation of electrical resistivity. *Rev. Mod. Phys.* **75**, 1085–1099 (2003).
16. Kim, D., Syers, P., Butch, N. P., Paglione, J. & Fuhrer, M. S. Coherent topological transport on the surface of Bi_2Se_3. *Nat. Commun.* **4**, 2040 (2013).
17. Xu, Y. et al. Observation of topological surface state quantum Hall effect in an intrinsic three-dimensional topological insulator. *Nat. Phys.* **10**, 956–963 (2014).
18. Chen, J. et al. Gate-voltage control of chemical potential and weak antilocalization in Bi_2Se_3. *Phys. Rev. Lett.* **105**, 176602 (2010).
19. Hikami, S., Larkin, A. I. & Nagaoka, Y. Spin–orbit interaction and magnetoresistance in the two dimensional random system. *Prog. Theor. Phys.* **63**, 707–710 (1980).
20. McCann, E. et al. Weak-localization magnetoresistance and valley symmetry in graphene. *Phys. Rev. Lett.* **97**, 146805 (2006).
21. Brahlek, M., Koirala, N., Salehi, M., Bansal, N. & Oh, S. Emergence of decoupled surface transport channels in bulk insulating Bi_2Se_3 thin films. *Phys. Rev. Lett.* **113**, 026801 (2014).
22. Steinberg, H., Laloë, J.-B., Fatemi, V., Moodera, J. S. & Jarillo-Herrero, P. Electrically tunable surface-to-bulk coherent coupling in topological insulator thin films. *Phys. Rev. B* **84**, 233101 (2011).
23. Liao, J. et al. Enhanced electron dephasing in three-dimensional topological insulators. *Nat. Commun.* **8**, 16071 (2017).
24. Brahlek, M., Koirala, N., Bansal, N. & Oh, S. Transport properties of topological insulators: band bending, bulk metal-to-insulator transition, and weak anti-localization. *Solid State Commun.* **215–216**, 54–62 (2015).
25. Ren, Z., Taskin, A. A., Sasaki, S., Segawa, K. & Ando, Y. Optimizing $Bi_{2-x}Sb_xTe_{3-y}Se_y$ solid solutions to approach the intrinsic topological insulator regime. *Phys. Rev. B* **84**, 165311 (2011).
26. Jozwiak, C. et al. Photoelectron spin-flipping and texture manipulation in a topological insulator. *Nat. Phys.* **9**, 293–298 (2013).
27. Jozwiak, C. et al. Spin-polarized surface resonances accompanying topological surface state formation. *Nat. Commun.* **7**, 13143 (2016).
28. Plucinski, L. et al. Robust surface electronic properties of topological insulators: Bi_2Te_3 films grown by molecular beam epitaxy. *Appl. Phys. Lett.* **98**, 222503 (2011).
29. Bianchi, M. et al. Coexistence of the topological state and a two-dimensional electron gas on the surface of Bi_2Se_3. *Nat. Commun.* **1**, 128 (2010).
30. Ishizaka, K. et al. Giant Rashba-type spin splitting in bulk BiTeI. *Nat. Mater.* **10**, 521–526 (2011).
31. Wang, X. & Chiang, T.-C. Topological states in Bi_2Se_3 surfaces created by cleavage within a quintuple layer: analysis in terms of the Shockley criterion. *Phys. Rev. B* **89**, 125109 (2014).
32. Edwards, S. F. The electronic structure of disordered systems. *Philos. Mag. J. Theor. Exp. Appl. Phys.* **6**, 617–638 (1961).
33. Olson, J. J. Anderson-McMillan prescription for the density of states of liquid iron. *Phys. Rev. B* **12**, 2908–2916 (1975).
34. Ryu, S. H. et al. Pseudogap in a crystalline insulator doped by disordered metals. *Nature* **596**, 68–73 (2021).
35. Korzhovska, I. et al. Spin memory of the topological material under strong disorder. *npj Quantum Mater.* **5**, 39 (2020).
36. Zallen, R. in *The Physics of Amorphous Solids* (ed. Zallen, R.) Ch. 1 (Wiley, 1998).
37. Brahlek, M. et al. Disorder-driven topological phase transition in Bi_2Se_3 films. *Phys. Rev. B* **94**, 165104 (2016).
38. Varjas, D. et al. Topological phases without crystalline counterparts. *Phys. Rev. Lett.* **123**, 196401 (2019).
39. Park, H. et al. Disorder-induced decoupled surface transport channels in thin films of doped topological insulators. *Phys. Rev. B* **98**, 045411 (2018).

Methods

Amorphous Bi_2Se_3 thin films were thermally evaporated in an ultrahigh vacuum chamber with a base pressure of 10^{-9} torr. The films were grown at room temperature from high purity (99.999%) elemental Bi and Se single sources (further growth and composition details are in Supplementary Note 1). The stoichiometry of the films was confirmed using X-ray photoelectron spectroscopy, energy dispersive X-ray spectroscopy and Rutherford backscattering spectroscopy. High-resolution TEM and FEM were performed on 10-nm-thick Bi_2Se_3 films deposited on a 10-nm-thick SiN window. FEM experiments were performed using an FEI TitanX operated at an acceleration voltage of 200 kV. Diffraction images were collected on an Orius charge-coupled device system with an exposure time of 0.3 seconds and a camera length of 300 mm. The probe convergence angle was set to 0.51 mrad by adjusting the third condenser lens current, resulting in a probe diameter of 2.2 nm and a probe current of 15.5 pA. Nanodiffraction data were collected as 15-by-15 image stacks (225 total images). Multiple 225-image datasets were collected for both the amorphous and polycrystalline Bi_2Se_3 for statistical averaging. Each dataset covered an area on the film of approximately 77 nm × 77 nm. The first image from each dataset was excluded to avoid including any potential sample damage or contamination in the data resulting from the parked beam. The central beam was covered using a beam stop and the beam position remained constant across all FEM images for each sample. Variations in peak position and intensity were negligible across data from different locations on a single film. Imaging conditions were held constant for all data collection to prevent variations in microscope alignment. The amorphous structure of the film was confirmed with X-ray diffraction, Raman spectroscopy and TEM.

The amorphous Bi_2Se_3 sample resistivity $\rho(T)$ was measured using a four-point probe. The samples were grown as a bar using a metal mask on predeposited Au(5 nm)/Cr(2 nm) contacts to ensure ohmic contact (shown in Fig. 2a inset). Magnetrotransport was measured in the van der Pauw configuration with samples grown onto predeposited Au(5 nm)/Cr(2 nm) contacts.

The Hamiltonian used to describe amorphous Bi_2Se_3 features direction-dependent spin–orbit hoppings set by the normalized hopping vector $\hat{\mathbf{d}}$ and is the sum of the on-site and hopping terms

$$H_{\text{onsite}} = m\sigma_0\tau_z, \tag{1}$$

$$H_{\text{hop}}(\hat{\mathbf{d}}) = it_1(\hat{\mathbf{d}}\cdot\boldsymbol{\sigma})\tau_x + t_2\sigma_0\tau_z \tag{2}$$

where σ_i and τ_i are the spin and orbital Pauli matrices, respectively; m sets the splitting between the local s- and p-like orbitals; t_1 is the spin–orbit hopping (the same as in Fig. 3); t_2 is the normal hopping amplitude; and i indicates an imaginary number. In the crystalline case this Hamiltonian correctly reproduces key features of the topologically non-trivial bands closest to the Fermi level[8]. We implement this tight-binding model on large systems of short-range correlated amorphous structures (Supplementary Fig. 3) and investigate the topological surface states by calculating spectral functions using the Kernel Polynomial Method[40,41].

We performed ARPES at the Advanced Light Source MAESTRO (7.0.2) and MERLIN (4.0.3) beamlines with photon energies in the range of 65–125 eV. ARPES results taken on different samples and at different beamlines are the same. The decap procedure does not create any crystalline order in our samples. The spin-resolved spectra were acquired from a high-efficiency and high-resolution spin-resolved time-of-flight spectrometer that uses the spin-dependent reflection from a magnetic thin film due to the exchange interaction[42]. The spin polarization is measured by the relative difference between spin-up and spin-down photoelectrons weighted by the Sherman function (S) of the detector, in the form $P_y = S \times (I_\uparrow - I_\downarrow)/(I_\uparrow + I_\downarrow)$. The light source for the spin measurements was a Lumeras 11 eV xenon gas-cell laser with 1 MHz repetition rate[43]. Synchrotron ARPES measurements and spin-resolved measurements were taken at 20 K and 75 K, respectively. ARPES was analysed using the PyARPES software package[44].

Density functional theory calculations were performed using the projector augmented-wave formalism in the Vienna Ab initio Simulation Package[45,46]. The exchange–correlation potentials were treated in the framework of the generalized gradient approximation of Perdew–Burke–Ernzerbof[47]. Bi (6s, 6p) and Se (4s, 4p) electrons were treated as valence, and their wavefunctions expanded in-plane waves to an energy cut-off of 500 eV. A k-point grid of 3 × 3 × 1 with gamma sampling was used. Spin–orbit coupling was added self-consistently for all density-of-states calculations. Amorphous structures were generated with ab initio molecular dynamics using the Vienna Ab initio Simulation Package.

Data availability

All data needed to evaluate the conclusions in the paper are present in the paper and/or the Supplementary Information. Additional data related to this paper may be requested from the authors.

References

40. Weiße, A., Wellein, G., Alvermann, A. & Fehske, H. The kernel polynomial method. *Rev. Mod. Phys.* **78**, 275–306 (2006).
41. Varjas, D., Fruchart, M., Akhmerov, A. R. & Perez-Piskunow, P. M. Computation of topological phase diagram of disordered $Pb_{1-x}Sn_xTe$ using the kernel polynomial method. *Phys. Rev. Res.* **2**, 013229 (2020).
42. Jozwiak, C. et al. A high-efficiency spin-resolved photoemission spectrometer combining time-of-flight spectroscopy with exchange-scattering polarimetry. *Rev. Sci. Instrum.* **81**, 053904 (2010).
43. He, Y. et al. Invited article: high resolution angle resolved photoemission with tabletop 11 eV laser. *Rev. Sci. Instrum.* **87**, 011301 (2016).
44. Stansbury, C. & Lanzara, A. PyARPES: an analysis framework for multimodal angle-resolved photoemission spectroscopies. *SoftwareX* **11**, 100472 (2020).
45. Kresse, G. & Furthmüller, J. Efficient iterative schemes for *ab initio* total-energy calculations using a plane-wave basis set. *Phys. Rev. B* **54**, 11169–11186 (1996).
46. Kresse, G. & Hafner, J. *Ab initio* molecular dynamics for liquid metals. *Phys. Rev. B* **48**, 13115–13118 (1993).
47. Perdew, J. P., Burke, K. & Ernzerhof, M. Generalized gradient approximation made simple. *Phys. Rev. Lett.* **77**, 3865–3868 (1996).

Acknowledgements

P.C. and S.C. thank E. Parsonnet and D. Rees for their discussions. A.G.G. is grateful to J. H. Bardarson, S. Ciuchi, S. Fratini and Q. Marsal for discussions. D.V. thanks A. Akhmerov, A. Lau and P. Perez Piskunow for discussions. The project was primarily funded by the US Department of Energy, Office of Science, Office of Basic Energy Sciences, Materials Sciences and Engineering Division under contract no. DE-AC02-05-CH11231 within the Nonequilibrium Magnetic Materials Program (MSMAG). The ARPES and spin-resolved ARPES work was supported by the Lawrence Berkeley National Laboratory's Ultrafast Materials Science programme, funded by the US Department of Energy, Office of Science, Office of Basic Energy Sciences, Materials Sciences and Engineering Division under contract no. DE-AC02-05-CH11231. TEM at the Molecular Foundry was supported by the Office of Science, Office of Basic Energy Sciences of the US Department of Energy under contract no. DE-AC02-05CH11231. Computational resources were provided by the National Energy Research Scientific Computing Center and the Molecular Foundry, US Department of Energy Office of Science User Facilities supported by the Office of Science of the US Department of Energy

under contract no. DE-AC02-05CH11231. The work performed at the Molecular Foundry was supported by the Office of Science, Office of Basic Energy Sciences of the US Department of Energy under the same contract. P.C. is supported by the National Science Foundation Graduate Research Fellowship under grant no. 1752814. S.C. was supported by the National Science Foundation Graduate Research Fellowship under grant nos DGE1852814 and DGE1106400. A.G.G. is supported by the French National Research Agency (ANR) under grant ANR-18-CE30-0001-01 and the European Union Horizon 2020 research and innovation programme under grant agreement no. 829044. D.V. is supported by Dutch Research Council (NWO) Vidi programme grant 680-47-53. S.Z. was supported by the National Science Foundation under STROBE grant no. DMR 1548924.

Author contributions

P.C. and S.C. contributed equally to this work. The project was initiated and overseen by P.C., S.C., A.G.G., A.L. and F.H.; P.C. grew the films. S.C. performed the synchrotron ARPES, S.C. and P.C. performed the spin-resolved ARPES measurements and S.C. performed the data analysis. P.C. performed the transport measurements. S.Z., E.K., S.C. and P.C. performed the TEM. M.M.-R. and P.C. performed the Raman measurements. Z.C. performed the molecular dynamics, and S.M.G. performed the density-of-states calculations. A.G.G. and D.V. constructed the tight-binding model, and D.V. performed the numerical calculations. P.C., S.C., A.G.G. and D.V. took part in interpreting the results. All authors contributed to writing the manuscript.

Competing interests

The authors declare no competing interests.

Additional information

Supplementary information The online version contains supplementary material available at https://doi.org/10.1038/s41563-022-01458-0.

Correspondence and requests for materials should be addressed to Paul Corbae.

Peer review information *Nature Materials* thanks Rob Moore, Benjamin Wieder and the other, anonymous, reviewer(s) for their contribution to the peer review of this work.